

# Impact of time-dependent non-axisymmetric velocity perturbations on dynamo action of von-Kármán-like flows.

André Giesecke\* and Frank Stefani

*Institute of Fluid Dynamics*

*Helmholtz-Zentrum Dresden-Rossendorf*

*POB 51 01 19, D-01314 Dresden, Germany*

Javier Burguete

*Departamento de Física y Matemática Aplicada*

*Universidad de Navarra*

*Irunlarrea 1, 31008 Pamplona, Spain*

(Dated: August 8, 2012)

## Abstract

We have performed numerical simulations of the kinematic induction equation in order to examine the dynamo efficiency of an axisymmetric von-Kármán-like flow subject to time-dependent non-axisymmetric velocity perturbations. The numerical model is based on the setup of the French Von-Kármán-Sodium dynamo (VKS) and on the flow measurements from a model water experiment conducted at the University of Navarra in Pamplona, Spain.

Our simulations show that the interactions of azimuthally drifting flow perturbations with the fundamental drift of the magnetic eigenmode (caused by the inevitable equatorial symmetry breaking of the basic flow) essentially determine the temporal behavior of the dynamo state. We find two distinct regimes of dynamo action that depend on the (prescribed) drift frequency of an ( $m = 2$ ) vortex-like flow perturbation. For comparatively slowly drifting vortices we observe a narrow window with enhanced growth-rates and a drift of the magnetic eigenmode that is synchronized with the perturbation drift. The resonance-like enhancement of the growth-rates takes place when the vortex drift frequency roughly equals the drift frequency of the magnetic eigenmode in the unperturbed system. Outside of this small window, the field generation is hampered compared to the unperturbed case, and the field amplitude of the magnetic eigenmode is modulated with approximately twice the vortex drift frequency. The abrupt transition between the resonant regime and the modulated regime is identified as an spectral exceptional point where eigenvalues (growth-rates and frequencies) and eigenfunctions of two previously independent modes collapse.

In the actual configuration the vortex drift frequency observed in the water experiment is much larger than the fundamental drift frequency of the magnetic eigenmode obtained from simulations and we conclude that the fulfillment of the resonance condition might be unlikely in present day dynamo experiments. Nevertheless, these radial vortices can be anchored to fixed spatial azimuthal positions (using holes or fingers) breaking the axisymmetry of the experimental setup. Moreover, a parametric resonance might occur in the Earth's core where tidal forcing provides appropriate flow perturbations, or in future dynamo experiments that will allow a better control of periodic non-axisymmetric velocity modes in order to meet the resonance condition.

PACS numbers: 47.65.-d, 91.25.Cw, 52.65.Kj

Keywords: kinematic dynamo simulations, dynamo experiment, parametric resonance

---

\* a.giesecke@hzdr.de

## I. INTRODUCTION

Cosmic magnetic fields are ubiquitous phenomena that are intrinsically coupled to most astrophysical objects like planets, stars or galaxies. The origin of these fields involves the formation of electrical currents by means of a complex flow of a conducting fluid or plasma. This process, the so called dynamo effect, is necessarily three dimensional and non-linear which makes an analytical or numerical approach difficult. Meanwhile, fluid flow driven generation of magnetic fields has also been obtained in laboratory experiments providing a complementary tool to astronomical observations or numerical simulations. However, whereas astrophysical dynamo action is comparably easy because of the large dimensions of the involved flows, its experimental realization requires considerable technical efforts [1]. An important obstacle for the occurrence of laboratory dynamo action arises from the scaling behavior of the power that is required to drive a flow with a requested magnetic Reynolds number  $Rm$ . For turbulent flows this power scales  $\propto Rm^3$  so that a reduction of the critical  $Rm$  for the onset of dynamo action is most important to achieve magnetic self-excitation at all.

So far dynamo experiments based on a flow of a conducting fluid have been successfully conducted in Riga [2], Karlsruhe [3] and Cadarache [4]. The first two facilities made use of a more or less predetermined fluid flow essentially fixed by the forcing and the shape of the internal tubes. Note, however, that at least in the Riga dynamo experiment the saturation process involved already a non-trivial back-reaction effect of the magnetic field that changes the geometry of the flow. Such effects might be even more pronounced in the Cadarache von-Kármán-sodium (VKS) dynamo. In that experiment the flow driving by two opposing impellers provides more freedom for the development of a saturated turbulent state, in which the back-reaction of the magnetic field on the fluid can strongly modify the geometry and dynamics of the flow. In an idealizing model the mean axisymmetric flow between counter-rotating impellers comprises two toroidal and two poloidal eddies (so called *s2t2* topology), and it is well known that this flow is able to drive a dynamo [5, 6]. Various attempts in different geometries have been made (numerically as well as experimentally) in order to examine dynamo action driven by such a flow [4, 7–20]. However, so far experimental dynamo action driven by a von-Kármán-like flow is obtained only at the VKS facility and only when at least one of the flow driving impellers is made of soft iron with a large relative permeability. Kinematic simulations of the Cadarache dynamo demonstrated the close linkage between the exclusive occurrence of dynamo action in the presence of soft iron impellers and the observed axisymmetry of the magnetic field [21, 22]. Nevertheless, a fully satisfactory explanation of the working principle of this dynamo is still missing and it is still unclear whether the present experiments will ever be able to achieve growing equatorial dipole modes, which constitute the originally expected magnetic field geometry.

An improvement of present numerical models may require the explicit consideration of coherent non-axisymmetric structures that repeatedly have been observed in water experiments using a von-Kármán-like flow driving [23–25]. Non-axisymmetric time-periodic flows with a dominant azimuthal wavenumber  $m = 2$  have also been found in 3D simulations of *s2t2* flows in spherical geometry [16]. Kinematic dynamo simulations using various manifestations of these velocity fields showed a surprising diversity of behavior patterns: self-generation of magnetic energy was only found when the time-dependent flow field was taken into account whereas the simulations with the time averaged flow or with different snapshots of the velocity field did not exhibit dynamo action.

The present paper aims at a numerical examination of the dynamo efficiency of a cylindrical VKS-like system subject to non-axisymmetric velocity perturbations with a single azimuthal wavenumber  $m = 2$ . Such velocity modes were observed in a water experiment conducted at University of Navarra in Pamplona in order to analyze the influence of slowly evolving large scale flow on the occurrence of dynamo action [23, 26]. In this study we utilize the essential features of the measured flow field as the basis input for numerical simulations of the kinematic induction equation. Typical input parameters that are systematically varied are the flow amplitude (in terms of the magnetic Reynolds number) and the azimuthal drift motion of the implied non-axisymmetric velocity perturbation. From the simulation data we extract the leading eigenmodes and the related eigenvalues in terms of growth-rates and frequencies that describe field amplitude modulations and/or azimuthal field drift. Interestingly, for comparably low drift frequencies of the velocity perturbation we first observe a phase locking of the magnetic eigenmode drift with the vortex drift which is replaced, for higher perturbation drift frequency, by the appearance of a time modulated magnetic eigenmode. By analyzing the involved growth rates and frequencies in the phase-locked regime and in the modulated regime, we identify the transition between them as a spectral exceptional point where eigenvalues and eigenfunctions of two modes coincide [27, 28]. The observed behavior is in close analogy with typical (resonant) mechanical systems subject to periodic forcing, like e.g. spinning disk systems [29] or to the behavior observed in the stability study of water waves [30]. Comparable effects have also been found in mean-field dynamos of  $\alpha\omega$ -type that were designed to explain the bisymmetric field pattern observed in spiral galaxies. In these models a periodic perturbation is caused by density waves due to spiraling arms, and a parametric resonance (also called *swing excitation*) is observed when the frequency of the perturbing velocity pattern is twice the oscillation frequency of the (axisymmetric) dynamo [31–35].

## II. EXPERIMENTAL BACKGROUND

The simulations presented below are motivated from a water experiment that is described in detail in [23]. In the experiment a von-Kármán swirling flow is driven by two counter-rotating impellers located at the end caps of a cylindrical vessel of radius  $R = 10$  cm and height  $H = 20$  cm (figure 1a). Both impellers spin with a rotation rate up to

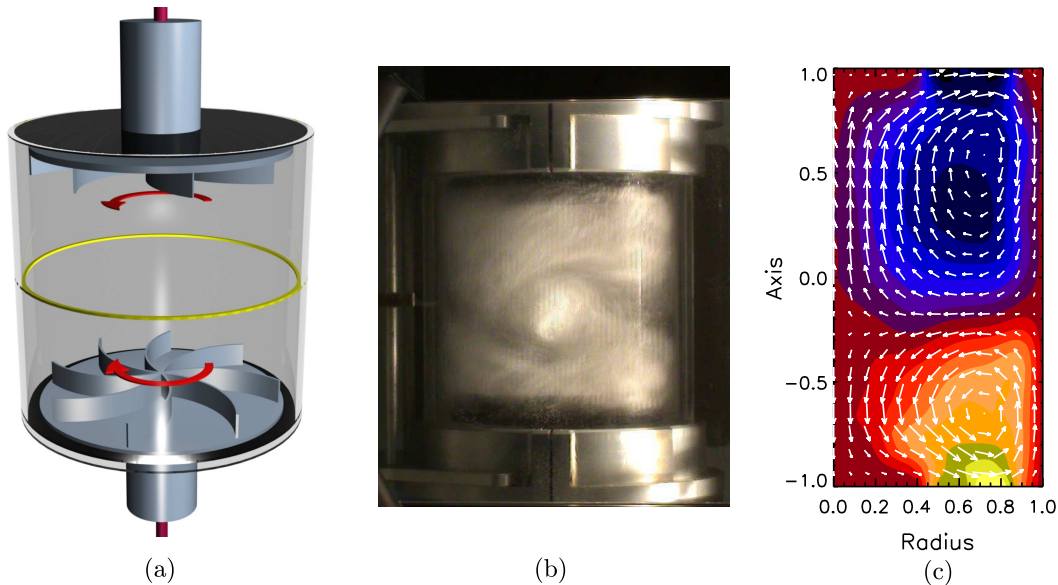


FIG. 1. (a) Sketch of the experimental setup. In the experiment the von-Kármán swirling flow is driven by two counter-rotating impellers located at the end caps of a cylindrical vessel of radius  $R = 10$  cm and height  $H = 20$  cm. The yellow ring denotes the equatorial plane of the cylinder. (b) Instantaneous snapshot of the turbulent fluid flow. Note the vortex like structure roughly in the center of the vessel. (c) Mean axisymmetric flow field measured in the experiment. The colored structure denotes the toroidal flow ( $u_\phi$ ) and the arrows denote the poloidal flow ( $u_r, u_z$ ). Although both impellers rotate with the same velocity different sizes of the flow cells occur due to spontaneous symmetry breaking.

12 Hz so that the resulting flow is highly turbulent with flow fluctuations of the same order as the mean flow (a typical snapshot of the turbulent flow is shown in figure 1b). The velocity field is measured using *Laser Doppler Velocimetry* (LDV) and the mean velocity field is obtained by averaging the instantaneous flow for (at least) 100 impeller turns. The resulting axisymmetric velocity field consists of two toroidal cells and two meridional recirculating cells that are roughly restricted to each cylindrical half-space (figure 1c). Comparable structures have been also observed in water experiments with similar configurations [24, 25]. The cylindrical configuration combined with the specific flow

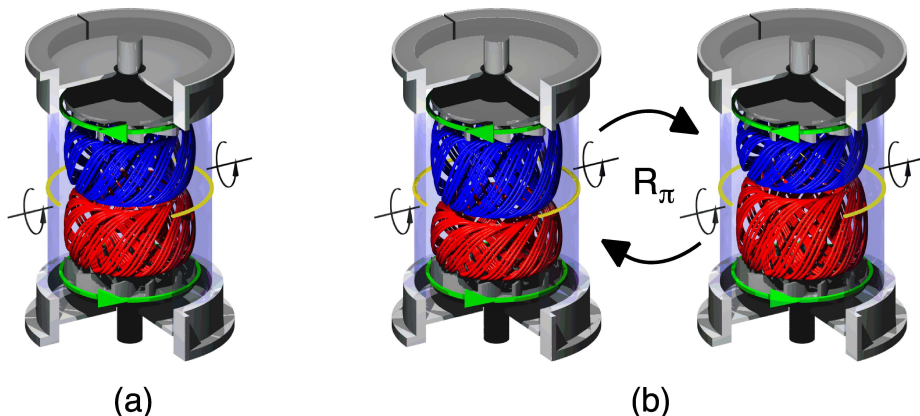


FIG. 2. Reconstruction of averaged trajectories in the experiment. The red and blue lines represent the averaged trajectories impelled by each one of the top and bottom impellers. (a) Symmetric flow configuration. (b) Equatorial symmetry breaking observed in the experiment when  $Re > 10^4$ . Spontaneous jumps between both possible states are observed in the experiment.

driving imposes a discrete symmetry: the most symmetric flow that can be obtained between two propellers rotating

in opposite directions breaks the reflection symmetry on any plane that contains the cylinder axis, but preserves the symmetry about a  $\pi$ -rotation around any diameter in the equatorial plane (figure 2a). However, in the water experiment this symmetry is broken for  $\text{Re} \gtrsim 10^4$  (without internal symmetrizing fixtures) and the measured mean velocity field becomes asymmetric even when both impellers spin with equal rotation rates [23]. As a consequence one of the cells (red or blue in figure 2b) becomes larger than the other. The averaged velocity field is meta-stable, and spontaneous jumps of the dominant cell from one side to the other are observed (so called *inversions*) with both possible states occurring with equal probability.

The transition time for an inversion is  $\tau_{\text{inv}} \approx 10$  s and the time between consecutive events varies from minutes to hours following a probability distribution  $\rho(t) = 1/T_0 e^{-t/T_0}$  with a parameter  $T_0$  determined by the noise intensity.  $T_0$  decreases for increasing Reynolds number, i.e. inversions occur more frequently if the turbulence is more vigorous. The inversions of the velocity field introduce a slow time scale at which the large scale flow and hence the large scale magnetic field change their structure. In the long run, the enhanced dissipation arising from the transition between different eigenstates (corresponding to the different velocity fields) can result in a reduced efficiency for the dynamo process when the mean life time of a velocity state becomes of the same order as the magnetic diffusion time [36].

In addition to breaking of the equatorial symmetry the observed mean flow also violates the ideal axial symmetry. Coherent non-axisymmetric structures emerge close to the equatorial plane (even before a turbulent state is reached) and establish a local swirling flow around an axis perpendicular to the main symmetry axis of the cylinder. The non-axisymmetric flow perturbation is dominated by an azimuthal wavenumber  $m = 2$  and undergoes an azimuthal drift that is immediately linked to the flow orientation of the dominating toroidal cell. The drift frequency of the vortex-like pattern is related to the maximum azimuthal mean flow velocity  $u_\varphi^{\text{max}}$  by  $\omega_v \approx 0.3 u_\varphi^{\text{max}} / R_v$ , where  $R_v$  denotes the radius of the maximum vortex velocity ( $R_v \approx 0.857$  in units of the cylinder radius). The mid-size structures provide an additional source of helicity, so that it is likely that the vortices are involved in the dynamo process when a conducting fluid like liquid sodium is utilized.

### III. NUMERICAL MODEL

The temporal development of the magnetic flux density  $\mathbf{B}$  induced from a flow  $\mathbf{u}$  of a conducting fluid is described by the magnetic induction equation that results from the combination of Faraday's law, Ohm's law and Ampère's law (without displacement current):

$$\frac{\partial \mathbf{B}}{\partial t} = \nabla \times (\mathbf{u} \times \mathbf{B} - \eta \nabla \times \mathbf{B}). \quad (1)$$

In (1)  $\eta$  denotes the magnetic diffusivity which is related to the electrical conductivity  $\sigma$  and the vacuum permeability  $\mu_0$  by  $\eta = (\mu_0 \sigma)^{-1}$ . Equation (1) is time stepped applying a finite volume method where a constraint transport scheme ensures the exact treatment of the solenoidal property of  $\mathbf{B}$  (if the initial field is divergence free). Insulating boundary conditions are treated with a modified boundary integral equation approach which yields the tangential field components on the boundary from the normal field components on the whole surface of the computational domain [37, 38].

#### A. The axisymmetric velocity field

We use an analytically prescribed flow field that incorporates the main characteristics of a von-Kármán flow and allows a convenient variation of the equatorial symmetry breaking. Since the typical life-time of the mean flow state is much longer than the time scales governing the (non-axisymmetric) flow perturbations the dynamics introduced by the inversions can be ignored so that we assume a time-independent axisymmetric velocity field. Equatorial symmetry breaking is modeled using a basic flow that is composed of two different axisymmetric parts with different symmetry properties. The main part is symmetric with respect to a  $\pi$ -rotation around any diameter in the equatorial plane. This contribution will be called *even flow* (figure 3a). The geometric structure of the even flow consists of two counter-oriented toroidal cells and two recirculating poloidal cells located in each cylindrical half-space. Mathematically, the

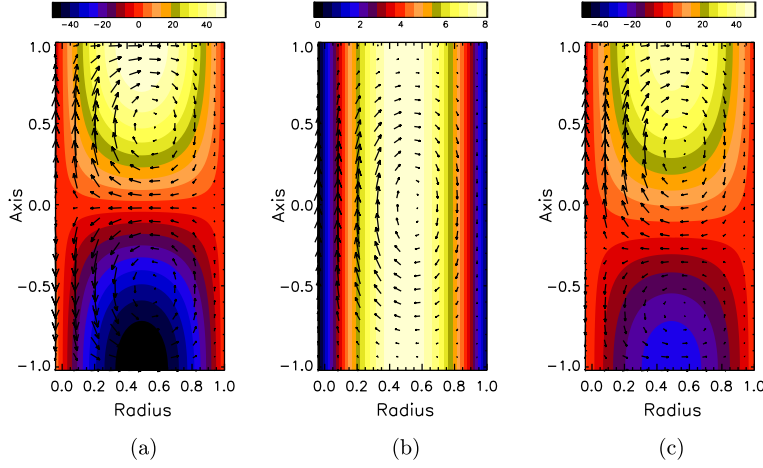


FIG. 3. Prescribed velocity field. From left to right: (a) even flow (MND flow) as given by equation (2), (b) odd flow contribution given by equation (3), (c) total flow  $\mathbf{u} = \mathbf{u}^e + a\mathbf{u}^o$  for  $a = 0.35$ . The color coded pattern represents the azimuthal flow ( $u_\varphi$ ) and the arrows denote orientation and magnitude of the meridional flow ( $u_r, u_z$ ).

even part is prescribed by the so called MND-flow first proposed by Marié, Normand and Daviaud [39]:

$$\begin{aligned} u_r^e(r, z) &= -\frac{\pi}{H}r(1-r)^2(1+2r)\cos\left(\frac{2\pi z}{H}\right), \\ u_\varphi^e(r, z) &= 4\epsilon r(1-r)\sin\left(\frac{\pi z}{H}\right), \\ u_z^e(r, z) &= (1-r)(1+r-5r^2)\sin\left(\frac{2\pi z}{H}\right), \end{aligned} \quad (2)$$

where  $\epsilon$  represents the relation between toroidal and poloidal flow (here  $\epsilon = 0.8155$ ) and  $H$  is the total height of the cylinder (here  $H = 2.0$ ).

The second contribution changes its sign when performing the same  $\pi$ -transformation and is called *odd flow* (figure 3b). This contribution is determined by a single poloidal cell that spreads through the whole cylinder and a global azimuthal rotation  $u_\varphi$  (independent of  $z$  and  $\varphi$ ). The odd flow contribution assumes the same expressions for  $\epsilon$ ,  $H$  and for the radial profile as used for the even flow (2) and is given by:

$$\begin{aligned} u_r^o &= \frac{\pi}{2H}r(1-r)^2(1+2r)\sin\left(\frac{2\pi z}{H}\right), \\ u_\varphi^o &= \epsilon r(1-r), \\ u_z^o &= (1-r)(1+r-5r^2)\cos^2\left(\frac{\pi z}{H}\right). \end{aligned} \quad (3)$$

The variation of the equatorial symmetry breaking is realized by multiplying the odd flow contribution (3) with a weighting factor  $a \in [0; 1]$  so that the total flow field is given by

$$\mathbf{u} = \mathbf{u}^e + a\mathbf{u}^o. \quad (4)$$

$\mathbf{u}$  describes a flow field with two different cell sizes with the even contribution always being dominant (see figure 3c). In our model the dominant toroidal eddy is always located close to the north (top) impeller (at  $z = +H/2$ ) and is characterized by a counterclockwise oriented azimuthal velocity (figure 3c).

The combined flow field is scaled allowing a systematically variation of the (prescribed) magnetic Reynolds number defined as

$$\text{Rm} = \frac{\mathcal{U}\mathcal{R}}{\eta}, \quad (5)$$

where  $\eta$  denotes the magnetic diffusivity,  $\mathcal{R}$  a characteristic length scale (here  $\mathcal{R} = 1$ , the radius of the cylindrical domain) and  $\mathcal{U}$  is the peak velocity defined by  $\mathcal{U} = U^{\max} = \max[(u_r^2 + u_\varphi^2 + u_z^2)^{1/2}]$ .

The flow field (4) is qualitatively similar to the model flow applied in [40] where dynamo action is examined in a VKS-like configuration with impellers rotating at different speeds. There are various other possibilities to realize the

equatorial symmetry breaking of the ideal flow field (2) and it turns out that not every property of the observed flow field can always be reproduced exactly. For example, the definition of the flow field (4) does allow an easy adjustment of the symmetry breaking in terms of the parameter  $a$ , but exhibits different azimuthal velocities near the impellers. In this sense the idealized flow (4) differs from the observed flow which results from a forcing through impellers that are in exact counter-rotation, so that the flow velocities close to both impellers are the same. Such deviations slightly influence the quantitative outcome of the simulations like e.g. the critical magnetic Reynolds number for the onset of dynamo action, nevertheless they do not affect the essential conclusions that will result from our simulations.

## B. Modeling of the non-axisymmetric velocity perturbations

The coherent non-axisymmetric flow perturbations are located near the outer wall of the cylinder and close to the equatorial plane where a strong shear layer emerges that is caused by the opposite azimuthal flow orientation in each cylindrical half. The vortices allow a relaxation of the shear in the equatorial layer in some way similar to a Kelvin-Helmholtz instability, but under turbulent conditions. The formation of the vortices in the experiment and the corresponding implementation in the numerical model are sketched in figure 4. In the simulations the vortices

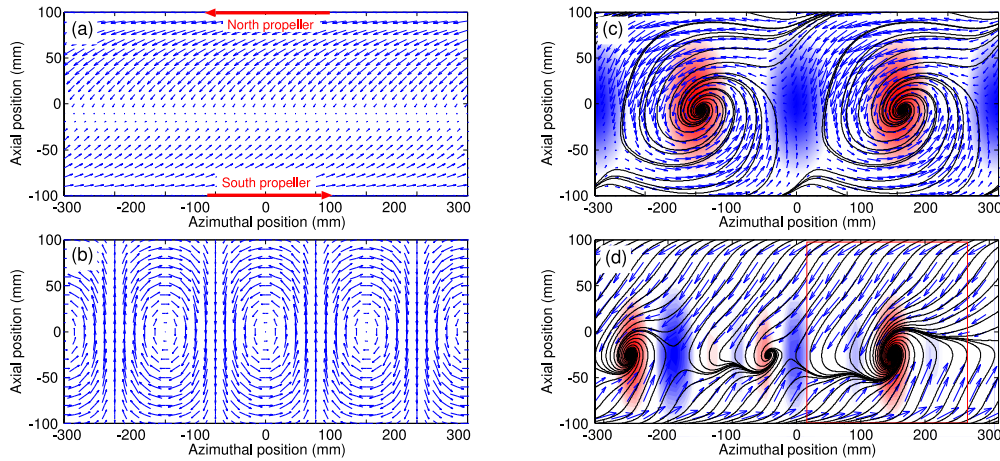


FIG. 4. Mean flow and vortex pattern realized in the model: The figures show axisymmetric and non-axisymmetric contributions of the velocity field in the  $(\varphi, z)$  plane at  $r = 0.9$ . Only the azimuthal and axial components of the velocity field are presented. (a) odd and even axisymmetric part (eqs. (2) and (3)). (b) Vortices according to (6) for  $m = 2$ . (c) Total velocity field (combining eqs. (2), (3) and (6)) for  $V_m = 0.2$ . The colored structures represent the radial component of the vorticity of the non-axisymmetric contribution  $(\nabla \times \mathbf{u}^v)_r$  (red (blue) corresponds to positive (negative) vorticity). (d) Same as in (c) for the experimental data.

are parameterized by analytical expressions whereby the essential properties – the azimuthal wave number, thickness, diameter and average radial position are taken from the measurements. The center of the vortices with a typical diameter of 0.5 (and an aspect ratio of unity) is located around the equatorial plane with a maximum at a radius of  $R_v = 0.857$  (all numbers are denoted in units of the cylinder radius  $R = 10$  cm). The non-axisymmetric contribution of the vortices to the velocity field is explicitly given by

$$\begin{aligned} u_r^v &= 0 \\ u_\varphi^v &= \frac{2V_m}{m} \cos(m(\varphi + \omega_v t)) r^2 (1 - r) e^{-[(r-r_0)/\sigma]^2} \sin(4z) \\ u_z^v &= -2V_m \sin(m(\varphi + \omega_v t)) r^2 (1 - r) e^{-[(r-r_0)/\sigma]^2} \cos^2(2z), \end{aligned} \quad (6)$$

with the axial coordinate  $z$  restricted to the interval  $z \in [-\pi/4; \pi/4]$ . In (6)  $V_m$  denotes the magnitude of the non-axisymmetric perturbation and the quantities  $\sigma$  and  $r_0$  are estimated from the experimental observations (here always  $r_0 = 0.9$  and  $\sigma = 0.12$ ). The azimuthal drift frequency of the vortex perturbation is denoted by  $\omega_v$ , which in the experiment is linked to the azimuthal velocity of the dominant mean flow cell. In the system of units applied in the simulations the observed vortex drift frequency  $\sim 0.3u_\varphi^{\max}/R_v$  corresponds to  $\omega_v \approx 17.1$  (14.9, 14.0, 13.1) for  $a = 0$  (0.62, 0.84, 1.00). Note that the drift frequency of the non-axisymmetric *velocity pattern* with an azimuthal wave number  $m$  is related to the previously defined vortex frequency by  $\Omega_p = m\omega_v$ . In the water experiment the



vortices exhibit an intermittent behavior, e.g. sudden jumps to a state with a different wavenumber ( $m = 3$  or  $m = 4$ ) or fluctuations of the vortex drift. Furthermore, the locations of the vortices undergo variations that are connected to the largest fluctuations of the mean velocity field. Those fluctuations appear centered around the shear layers, and close to the wall. These temporal alterations are not considered in our numerical model, where we restrict our examinations to the case  $m = 2$  which corresponds to the most probable configuration observed in the experiment. In all cases the disturbance introduced by the non-axisymmetric component remains only weak and has no influence on the actual Rm given by the maximum of the modulus of  $\mathbf{u}$ .

#### IV. RESULTS

In the kinematic approach the back-reaction of the magnetic field on the flow is neglected so that the solution of the induction equation (1) represents a linear problem, which in principle could be solved with the Ansatz  $\mathbf{B}(\mathbf{r}, t) = \mathbf{B}_0(\mathbf{r})e^{\lambda t}$ . A dynamo solution is obtained if the magnetic energy density  $E_{\text{mag}} = (2\mu_0)^{-1}|\mathbf{B}|^2$  grows exponentially  $\propto e^{2\lambda t}$ . In general  $\lambda$  is a complex quantity  $\lambda = \gamma + i\omega$  where  $\gamma$  denotes the field amplitude growth rate and  $\omega$  denotes an oscillation or drift frequency. In accordance with Cowling's anti-dynamo theorem, dynamo solutions generated by a prescribed mean axisymmetric flow necessarily yield a non-axisymmetric field. In all simulations presented below the ( $m = 1$ ) mode is the dominant field contribution so that the magnetic eigenmode behaves  $\propto \cos\varphi$  and represents a dipole oriented along the equatorial plane. This is in contrast to the real VKS experiment in which the presence of the magnetic impellers works in favor of an axisymmetric eigenmode (axial dipole, [21, 22]). In the following the growth rates represent magnetic field amplitude growth rates for this ( $m = 1$ ) mode and the applied time scale is given by the magnetic diffusion time  $\tau_\eta = R^2/\eta$ .

##### A. Equatorial symmetry breaking

For a sufficiently large magnetic Reynolds number the flow field (4) drives a dynamo with a typical structure shown in figure 5 which displays the eigenmodes for the undisturbed flow field ( $a = 0$ ) and the model case  $a = 0.62$ . In both cases the geometry is dominated by two interleaved banana-cell like structures. However, in case of equatorial symmetry breaking ( $a = 0.62$ , right panel) a slight concentration of magnetic energy is observed in the upper cylindrical half-space containing the dominant flow cell. The breaking of the ideal equatorial symmetry suppresses dynamo action: when a symmetry breaking flow contribution is added the critical magnetic Reynolds number for the onset of dynamo action roughly increases  $\propto a^2$  from  $\text{Rm}^c \approx 50.5$  for  $a = 0$  to  $\text{Rm}^c = 109.5$  at  $a = 1$  (figure 6a & b).

In the ideal symmetric case ( $a = 0$ ) the eigenmode shows no time dependence except the exponential decay. With symmetry breaking the ( $m = 1$ ) mode exhibits an azimuthal drift around the cylinder axis, i.e.  $\mathbf{B} \sim$

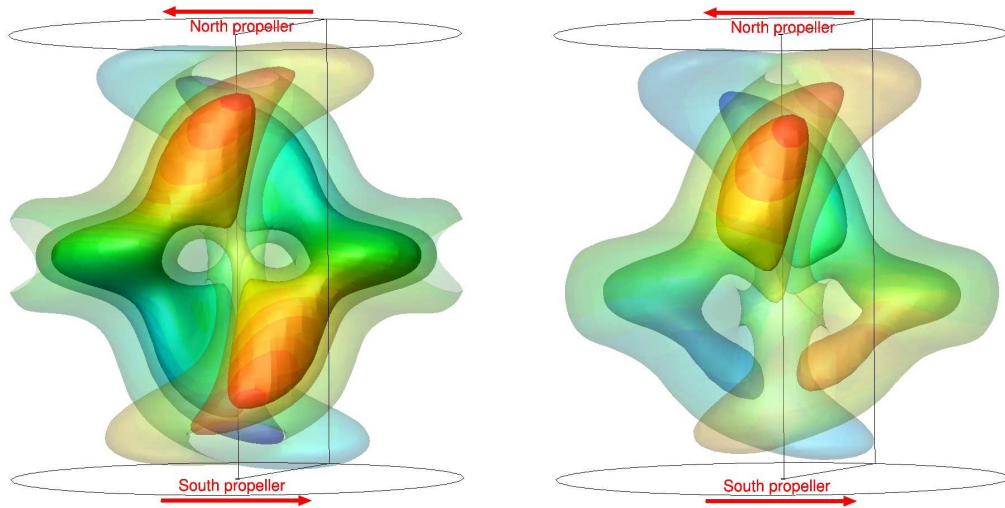


FIG. 5. Geometric structure of the dynamo eigenmode. Left: no equatorial symmetry breaking ( $a = 0$ ),  $\text{Rm} = 70$ . Right:  $a = 0.62$ ,  $\text{Rm} = 70$ . The isosurfaces show the magnetic energy density at 10%, 30% and 50% of the respective maximum value. The colored contours denote the azimuthal magnetic field  $B_\varphi$ . Note the magnetic energy concentration in the upper part of the cylinder which contains the dominant flow cell in case of equatorial symmetry breaking (right panel).

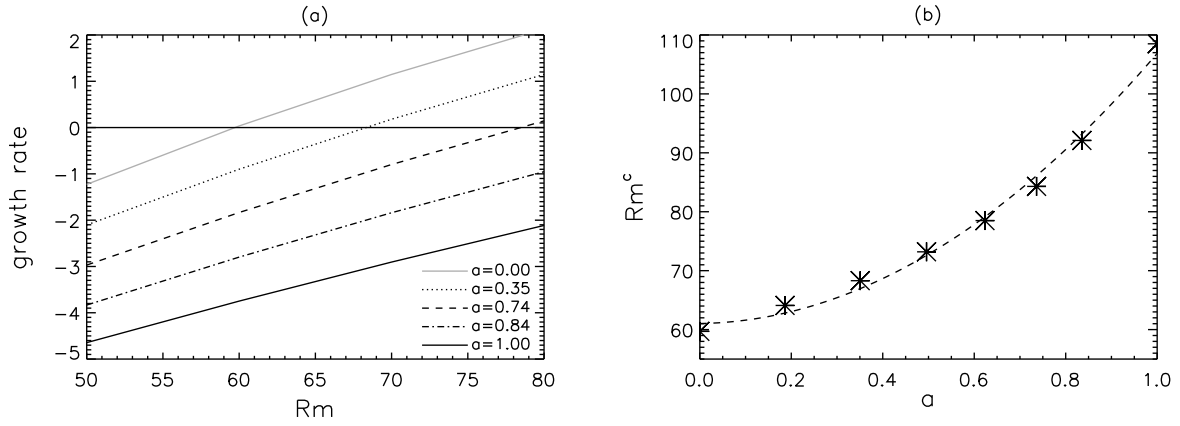


FIG. 6. (a) Growth-rate versus  $Rm$  for various equatorial symmetry breaking  $a$ ; (b) critical magnetic Reynolds number versus  $a$ . The dashed curve denotes a fit by a polynomial of degree 2.

$B_0(r, z)e^{\lambda t} \cos(\varphi - \omega_f t)$  with the magnetic field drift frequency  $\omega_f$  increasing nearly linearly with the degree of asymmetry  $a$  and with  $Rm$  (figure 7a & b).  $\omega_f$  is constant in time and is oriented opposite to the azimuthal flow in the dominant cell. For axisymmetric velocity fields (as  $\mathbf{u}^e$  and  $\mathbf{u}^o$ , eqs 2 & 3) poloidal and toroidal velocity components are decoupled, and their shear layer may have independent locations. The relative position of these shear layers controls the magnitude (and orientation) of the magnetic field drift. For example, an exclusive increment of the odd azimuthal flow contribution (which only shifts the toroidal shear layer) would alter the drift frequency. The change might be quite dramatic and even a reversal of the drift orientation is possible with the eigenmode co-rotating with the dominant azimuthal flow, as observed for example in [8]. A systematic study of the influence of this effect is under way.

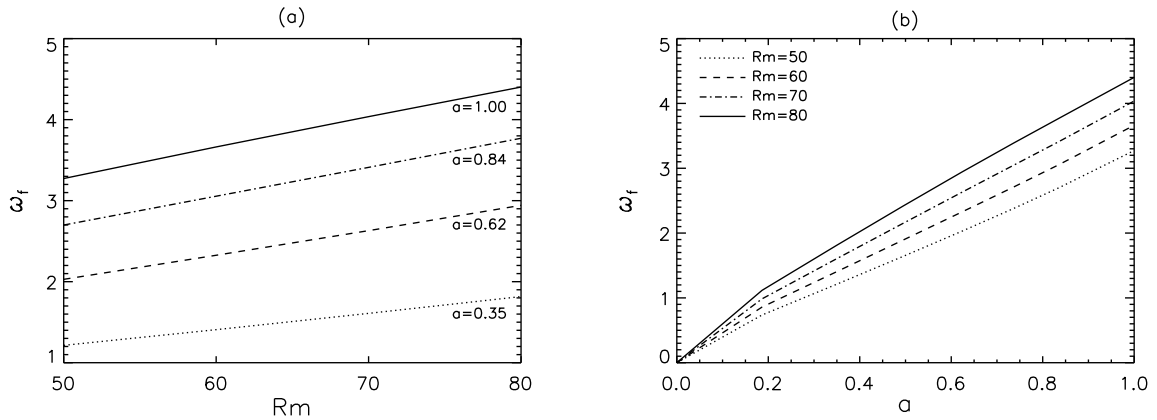


FIG. 7. (a) Drift frequency of the ( $m = 1$ ) mode versus  $Rm$  for various  $a$ . (b) drift frequency of the ( $m = 1$ ) mode versus equatorial symmetry breaking  $a$ . Note the slight deviation from the linear behavior for small  $a$ .

## B. Impact of non-axisymmetric velocity perturbations

The presence of non-axisymmetric velocity components results in a coupling between different azimuthal magnetic field modes that are separated in the purely axisymmetric problem. Hence the characterization of the dynamo eigenmode with a single azimuthal wavenumber is no longer correct because (in principle) all azimuthal wave numbers are linked. In the following, we examine the impact of a non-axisymmetric flow perturbation with a (single) wave number  $m = 2$  so that two classes of magnetic eigenmodes arise which incorporate even azimuthal wave numbers ( $m = 0, 2, 4, \dots$ ), or odd azimuthal wave numbers ( $m = 1, 3, 5, \dots$ ), respectively. In our model only the second class with odd wave numbers is relevant whereas the "even modes" decay on a much faster timescale.



In the following, we keep the amplitude of the non-axisymmetric velocity contribution fixed at  $V_m = 0.3U^{\max}$  which roughly corresponds to the value observed in the experiments. In this regime the presence of the non-axisymmetric velocity component neither changes the global (axisymmetric) flow topology nor the actual magnetic Reynolds number. We further assume that the drift frequency of the vortex,  $\omega_v$ , is a free parameter that is systematically varied in the interval  $\omega_v \in [-60, +60]$ . The maximum/minimum values correspond to a vortex drift *velocity* approximately equal to the maximum azimuthal flow velocity (recall that in the water experiment the observed vortex drift velocity is roughly  $0.3u_\varphi^{\max}$ ). We also examined the artificial case with a vortex drift orientation opposite to the azimuthal flow of the dominant cell. These cases are denoted by negative frequencies. The temporal development of the amplitude of

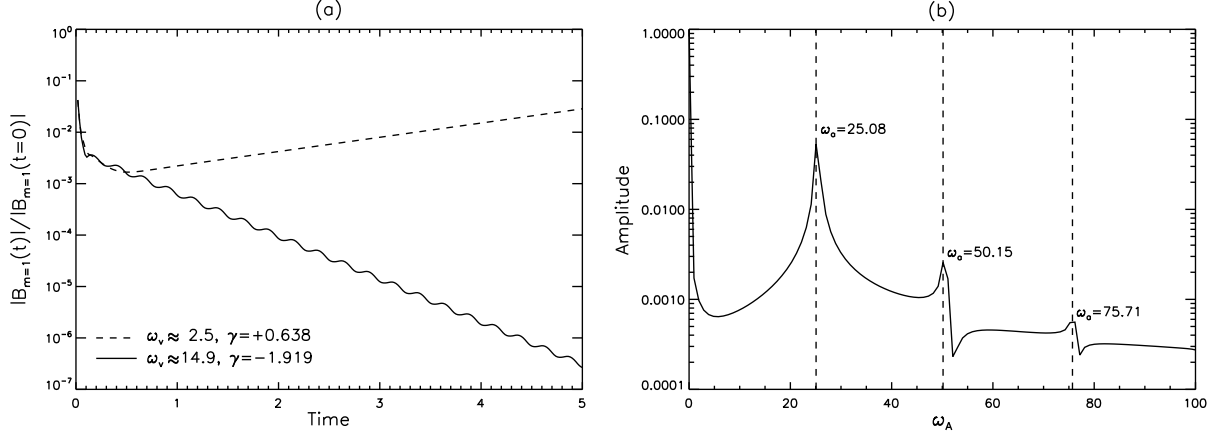


FIG. 8. (a) Time dependence of the magnetic field amplitude for  $Rm = 70$  and  $a = 0.62$ . (b) Fourier spectrum for the case  $\omega_v = 14.9$  (after eliminating the exponential decay). The various peaks denote the modulation frequency of the field amplitude  $\omega_a \approx 25.08$  (and its overtones).

the dominant eigenmode for two different vortex drift frequencies, but similar  $Rm$ , is shown in figure 8 (dashed curve:  $\omega_v \approx 2.5$ , solid curve:  $\omega_v \approx 14.9$ ). Both curves show completely different behavior: for  $\omega_v \approx 14.9$  the solution decays and its amplitude is modulated with a frequency of  $\omega_a \approx 25.08$  (solid curve), whereas for  $\omega_v \approx 2.5$  the field amplitude does not show any time dependence except the exponential growth (dashed curve). Regardless of the distinct temporal behavior for both cases the field structure is quite similar (except the pulsating character in the modulated case) and remains close to the pattern already observed in the previously discussed unperturbed configuration (figure 9).

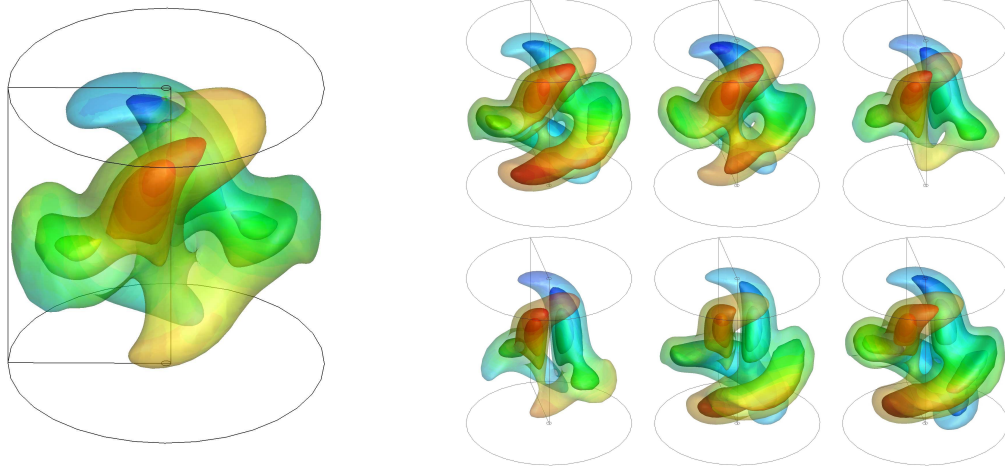


FIG. 9. Left: field structure in the resonant regime ( $Rm = 70, a = 0.62, \omega_v = 2.5$ , corresponding to the dashed curve in the left panel of figure 8). Right: time series of a typical solution with amplitude modulation ( $Rm = 70, a = 0.62, \omega_v \approx 14.9$ , corresponding to the solid curve in the left panel of figure 8). The isosurfaces show the magnetic energy density at 10%, 30% and 50% of the respective maximum value and the colored contours denote the azimuthal magnetic field  $B_\varphi$ . The time series covers one modulation period with each snapshot scaled by the respective maximum so that the effects of exponential decay/growth and the amplitude modulations are eliminated. The period of the amplitude modulation is much shorter than the time scale of the magnetic field drift so that the phase of the eigenmode (i.e. its orientation in space) remains nearly constant.

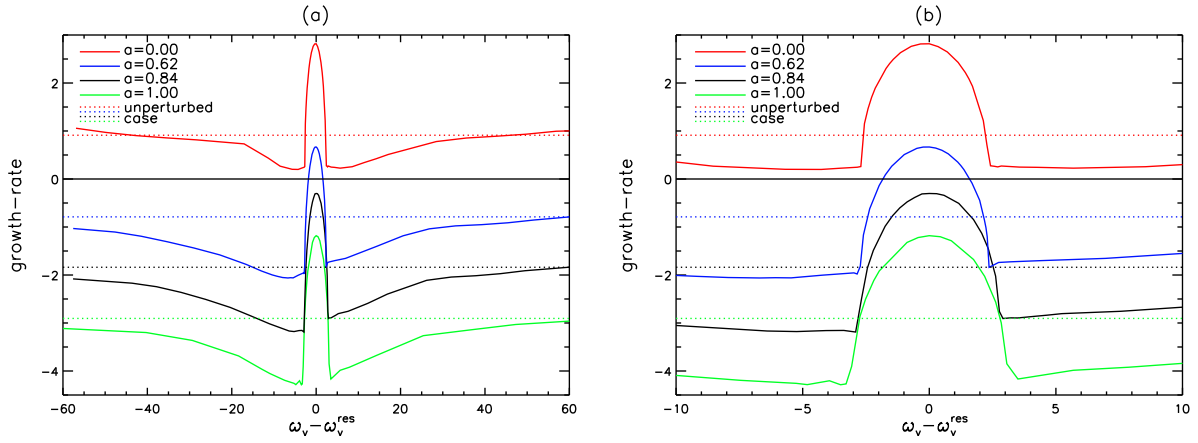


FIG. 10. (a) Growth-rate versus vortex drift frequency for  $Rm = 70$  and  $V_m = 0.3U^{\max}$ . In the abscissa the resonance frequency  $\omega_v^{\text{res}}$  has been subtracted so that all curves are centered at the origin. The horizontal dotted lines denote the growth rates without non-axisymmetric perturbation. (b) enlarged section of the resonant regime. The growth-rates in the resonant regime correspond to non-oscillating  $m = 1$  eigenmodes whereas outside of this window the solutions exhibit a modulation of the field amplitude (see also figure 11c).

The occurrence of non-axisymmetric solutions with oscillating energy is a clear indication for the presence of two distinct azimuthal modes with the same growth-rate (i.e. real part of the eigenvalues) but with different frequencies (imaginary part of eigenvalues). In fact simulations that cover a sufficient number of periods exhibit characteristic beat patterns indicating that the frequencies of the superimposed modes are very close. We observe field amplitude modulations independently of the degree of equatorial symmetry breaking for a broad range of vortex drift frequencies, whereas unmodulated solutions only occur within a narrow window of relatively slow vortex drift frequencies. The unmodulated solutions are further characterized by a sharp maximum for the corresponding growth-rates (figure 10), typical for parametric resonance. Characteristic properties of the resonant regime and a comparison to values in the unperturbed state are denoted in table I. The location of the resonance maximum (denoted by  $\omega_v^{\text{res}}$ ) is roughly

TABLE I. Characteristics properties of the resonant window for different values of the equatorial symmetry breaking  $a$ . All data stems from runs with  $Rm = 70$ . The critical magnetic Reynolds number (column 6 & 7) has been estimated from inter/extrapolation of simulation runs with  $Rm = 50, 70$  and  $90$ .

$a$	maximum growth rate	$\omega_v^{\text{res}}$	unperturbed growth rate	$\omega_f^0$	$Rm^c$ without vortex	$Rm^c$ at resonance	relative reduction of $Rm^c$	width of unmodulated regime $\Delta\omega_v$
0.00	+2.817	-0.00	+0.912	0.00	59.7	50.5	15.4%	5.06
0.62	+0.667	-1.99	-0.798	-2.63	78.5	64.8	17.5%	5.11
0.84	-0.302	-2.91	-1.839	-3.41	92.1	72.9	20.8%	5.63
1.00	-1.181	-3.50	-2.905	-4.04	108.5	82.7	23.8%	6.12

determined by the field drift frequency of the magnetic eigenmode in the unperturbed case (from now labeled with  $\omega_f^0$ ). However, a constant gap is observed in runs with equatorial symmetry breaking ( $a > 0$ ) resulting in  $\omega_v^{\text{res}} \approx (\omega_f^0 + 0.5)$ , whereas the case  $a = 0$  remains a particular case with  $\omega_v^{\text{res}} = 0$ . The shift of the resonance frequency with respect to the fundamental frequency in the unperturbed problem probably follows from the interaction of vortex structure and *drifting* eigenmode similar to the shift of the resonance frequency in periodically forced mechanical systems with damping. Outside of the resonance, the growth-rate is suppressed compared to the unperturbed case (denoted by the dotted horizontal line in figure 10). Only for very large drift velocities the value of the purely axisymmetric case is obtained again, i.e. the impact of the vortices vanishes when their drift frequency becomes too large. The width of the resonant regime slightly increases with the symmetry breaking parameter  $a$  and so does the relative enhancement of the growth-rates and accordingly the relative reduction of the critical  $Rm$ .

The periodic distortion caused by the drifting vortices also influences the drift behavior of the magnetic eigenmode. In the resonant regime the dynamo eigenmode exhibits an azimuthal field drift that is immediately locked to the vortex drift frequency, i.e. the magnetic field pattern follows the vortices ( $\omega_f \sim \omega_v$ , figure 11b). This frequency locking also applies without equatorial symmetry breaking ( $a = 0$ ) which does not show any field drift without vortices (red curve

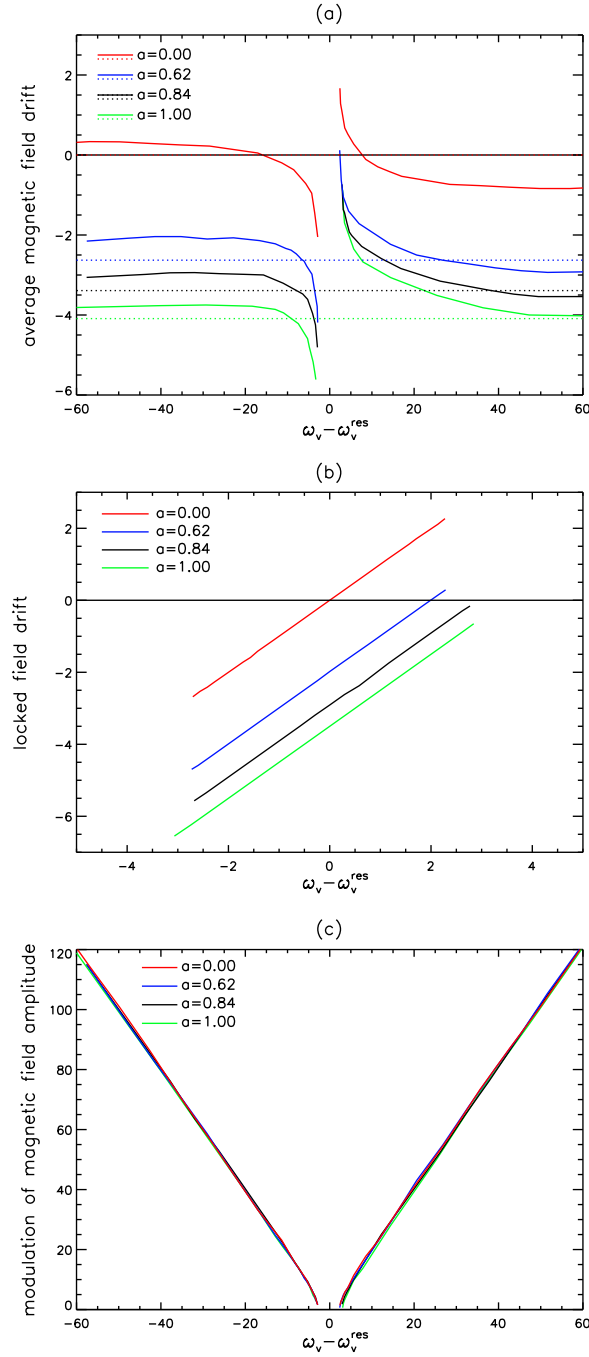


FIG. 11. (a) average field drift frequency versus the vortex drift frequency for various values of the symmetry breaking parameter  $a$ . The solid curves denote the average field drift in the modulated regime. The horizontal dotted lines denote the field drift in the unperturbed case ( $\omega_f^0$ ). (b) field drift frequency in the resonant regime. The field drift is synchronized with the vortex drift:  $\omega_f \sim \omega_v$ . (c) field amplitude modulation for various values of the symmetry breaking parameter  $a$ . The amplitude modulations scales  $\omega_a \sim 2\omega_v$ .

in figure 11b). Beside the temporal decay/growth, the (constant) azimuthal field drift determines the only time scale in the resonant regime, whereas outside of the resonant window two different time scales appear: an average azimuthal field drift that is roughly determined by the equatorial symmetry breaking parameter  $a$  (solid curves in figure 11a)<sup>1</sup>

<sup>1</sup> This does not hold in the vicinity of the transition between the modulated regime and the resonant regime where the field drift exhibits a divergent trend.

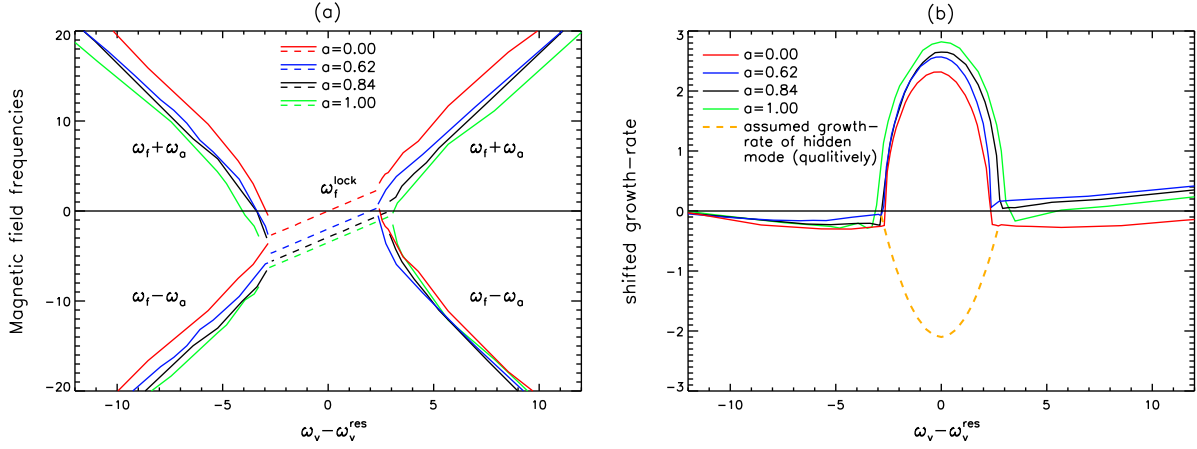


FIG. 12. (a) compilation of frequencies of the magnetic eigenmode versus the vortex drift frequency minus the resonance frequency. The solid curves show a combination of field drift and field amplitude modulation and the dashed central part denotes the field drift locked to the vortices in the resonant regime. (b) corresponding growth-rates, Note the dashed curve in the bottom part which represents the assumed growth-rates of a *hidden* mode that cannot be identified with the applied time-stepping approach.

and the aforementioned modulation of the field amplitude which scales  $\sim 2\omega_v$  (figure 11c). In the modulated regime the field drift is not constant but varies regularly with the same timescale as the amplitude modulation. A movie that shows the time development of four characteristic runs (no vortex, resonant run with frequency locking and modulated case with positive and/or negative vortex drift frequency) can be found in the supplemental material for this article [41].

In order to illustrate the behavior of the eigenmode in the vicinity of the transition between the resonant and the modulated regime we have combined the curves shown in figure 11 into one drawing. Figure 12 shows a combination of frequencies of the magnetic eigenmode ( $\omega_f + \omega_a$  and  $\omega_f - \omega_a$ , left panel) and the related growth-rates (right panel) against  $\omega_v - \omega_v^{\text{res}}$ . By using the sum/difference of the observed frequencies (drift and amplitude modulation) a continuous transition but with a jump in the derivative is achieved between modulated and resonant regime. For larger vortex drift, the behavior is dominated by the amplitude modulation, whereas close to the transition (where  $\omega_a \rightarrow 0$ ) the behavior is determined by the field drift frequency  $\omega_f$ .

The abrupt transition from the modulated regime with  $\omega_a \sim 2\omega_v$  to an unmodulated regime with  $\omega_a = 0$  and  $\omega_f \sim \omega_v$  occurs when two different eigenmodes merge. At these points, known as *exceptional points* [27], the eigenvalues of two eigenmodes coincide. In our case the change of the temporal behavior of the eigenmode results from the merging of the imaginary parts of the two eigenvalues whereas the real parts (growth-rates) are identical in the modulated regime giving rise to the field amplitude modulation. In the resonant regime (where the field amplitude modulation vanishes) the real parts of the eigenvalues of both interacting modes split and presumably form a "bubble" similar to the behavior of periodical perturbed resonant mechanical systems (see discussion below). In addition, at the exceptional point the two previously linearly independent eigenfunctions collapse and become indistinguishable. Mathematically this is described by the formation of a non-diagonal Jordan block structure in the matrix representation of the (non-selfadjoint) dynamo operator associated with algebraic eigenvectors [42]. A characteristic property of exceptional points with two coinciding eigenvalues is reflected in the time dependence of the field amplitude which, exactly at the exceptional point, exhibits an additional secular term linear in  $t$  [43] so that

$$\mathbf{B}(t) \sim (\mathbf{b}_1 + \mathbf{b}_2 t) e^{\gamma t}. \quad (7)$$

Such a time dependence has been found experimentally in an examination of a two level system in microwave billiards [44] and it would be interesting to identify this term in our simulations. However, up to present, the determination of growth-rates and frequencies near the transition from the modulated solution to the resonant solution is difficult and did not allow a reliable and unique determination of such a state. Hence, we can only speculate on the nature of the interacting eigenmodes because, unfortunately, with our present time-stepping method, we can only identify the leading eigenmode, whereas the identification of the second mode would require the use of an appropriate eigenvalue solver. However, it is rather suggestive to assume that the leading mode essentially consists of a dominant ( $m = 1$ ) component with some slight addition of a ( $m = 2$ )-vortex induced ( $m = 3$ ) component, and that the second eigenmode is dominated by a ( $m = 3$ ) component, to which a slight ( $m = 2$ )-vortex induced ( $m = 1$ ) component is added. Independently, we expect that the growth-rates of this "hidden" mode qualitatively behaves in the same way as in

comparable mechanical systems forming a bubble in the resonant regime. The assumed development has been added in figure 12 in terms of the dashed orange curve. This behavior is known e.g. from mechanical systems subject to periodic perturbations, the stability analysis of water waves conducted in [30] or the response of a non-linear state to spatially periodic forcing examined in [45]. A comparable pattern is also observed in the eigenvalue spectrum of oscillating  $\alpha^2$ -dynamos with non-trivial radial distribution of  $\alpha$  [46, 47]. However, in those models the behavior of the growth-rates and the frequencies is exchanged: the real part of the eigenvalues merge/split (in the same manner as the frequencies in the left panel of figure 12) and the imaginary parts form a bubble corresponding to a restricted regime with oscillatory (axisymmetric) solutions with two conjugate complex eigenvalues. In particular, the aforementioned mechanical examples can often be described by a Mathieu equation

$$\ddot{x} + (a - \delta \cos(2t))x = 0, \quad (8)$$

where  $x$  denotes an oscillating state,  $a$  is related to the fundamental frequency of the system and  $\delta$  is the amplitude of the periodic perturbation (e.g. pendulum with vertical oscillations of their pivot, fast spinning disks with time-varying loads [29]). However, the dynamo problem can be reduced to a Mathieu-like equation only in a few simplifying cases. For example, the thin disk approximation used in the galactic  $\alpha\omega$ -model from [31] allows a description of the amplitude of the magnetic vector potential by an equation similar to (8). A parametric resonance (also called *swing excitation*) is observed when the frequency of the perturbing velocity pattern is twice the natural frequency of the dynamo. Likewise, parametric resonances have been found in a Bullard-type disc dynamo model with a periodic modulation of the disc rotation. The model is based on a damped variant of (8) and resonances which allow magnetic field excitation for rather low velocities of the conducting disc are also observed at higher frequencies [48]. A more general description for systems subject to periodic distortions is given by

$$\dot{\mathbf{x}}(t) = \mathbf{M}(t)\mathbf{x}(t) = (\mathbf{A} + \mathbf{B} \sin \omega t)\mathbf{x}(t) \quad (9)$$

where  $\mathbf{x}$  is the departure from a basic state,  $\mathbf{M}(t)$  is periodic with the forcing period  $T = 2\pi/\omega$  and  $\mathbf{A}$  is an operator that describes the unperturbed system. In principle, equation (9) is suitable to describe the system examined in the present study (with  $\mathbf{A}$  denoting the unperturbed dynamo operator). However, without detailed (analytical) knowledge of the eigenvalues and eigenvectors of the unperturbed problem an analytical treatment remains impossible, so that here we restrict ourselves to a qualitative description of the fundamental approach. The general form for the solution of system (9) follows from Floquet theory and is given by  $\mathbf{x}(t) \sim \sum_i e^{\mu_i t} \mathbf{P}_i(t)$ , where  $\mathbf{P}_i(t)$  has the period  $T$  and  $\rho_i = e^{\mu_i t}$  are the so called *Floquet multipliers* (e.g. [49, 50]). It can be shown that the computation of eigenvalues and eigenvectors of the problem yields different regimes that are characterized by stable, unstable, periodic or pseudo periodic solutions with simple and double periodicity in accordance with the frequency scaling in the modulated and/or resonant regime that is obtained in our study. Furthermore, a general calculation of the Floquet exponents  $\mu_i$  immediately explains the occurrence of exceptional points where eigenvalues and eigenvectors coincide. Concerning our present study, however, neither a reduction to a Mathieu-like equation nor an analytical computation of the Floquet exponents is possible without severe simplifications so that we abandon from further quantitative discussions at this stage.

The observed behavior can also be explained on the basis of simple physical principles. For sufficiently slowly drifting vortices the system adjusts itself to an optimum state and the (azimuthal) phase between magnetic eigenmode and vortex pattern remains fixed so that the field growth becomes maximal. This state is essential characterized by the alignment between the magnetic eigenmode and the non-axisymmetric velocity mode which is roughly the same independently of symmetry breaking or vortex drift (see figure 13). Increasing  $\omega_v$ , the magnetic eigenmode cannot follow the ever faster ( $m = 2$ ) vortex drift, but "bethinks" of its own eigenvalue (in the unperturbed state) to which it converges in the limit  $|\omega_v| \rightarrow \infty$ . In doing so, it will be "beaten" by the  $m = 2$  vortex mode with an ever increasing frequency  $2\omega_v$ , which explains the occurrence of the second frequency involved.

## V. CONCLUSIONS

We have examined kinematic dynamo action of a von-Kármán like flow of a conducting fluid in a cylindrical container. When the flow breaks the ideal equatorial symmetry of the system, the critical magnetic Reynolds number for the onset of dynamo action increases with the amount of symmetry breaking and a time dependence is introduced in terms of an azimuthal drift motion of the dominant dynamo eigenmode. The frequency of this drift increases with the amount of symmetry breaking as well as with the magnetic Reynolds number.

The main focus of our examinations has been on the interaction of this field drift with a non-axisymmetric time-dependent velocity perturbation and the resulting impact on dynamo action. In summary, what we observe is the following: the temporal behavior of the system is governed by three different time scales: the decay/growth time,

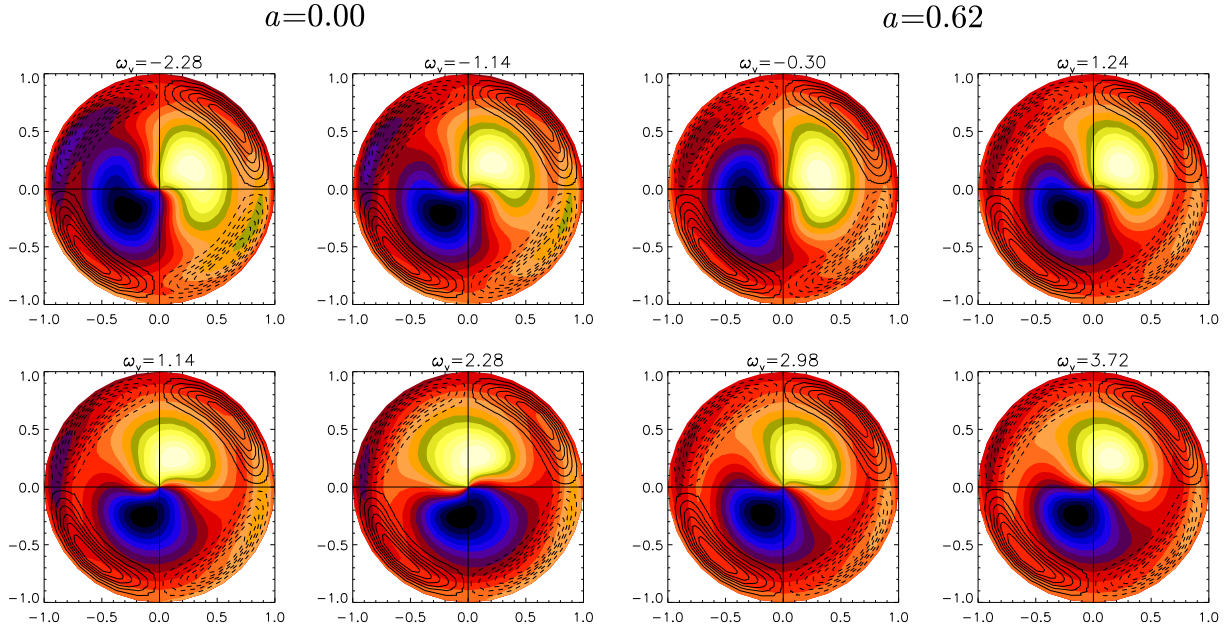


FIG. 13. Alignment of magnetic eigenmode and velocity perturbation for different values of the vortex drift frequency  $\omega_v$ . All runs stem from the resonant regime. The color coded structure denotes  $B_\varphi$  and the contour lines show the axial velocity perturbation  $u_z^v$ . Left:  $a = 0$ , right:  $a = 0.62$

the magnetic field drift and the vortex drift which, in contrast to the first two represents an imposed quantity. For rather slow vortex drift frequencies, the first magnetic eigenmode (dominated by an  $(m = 1)$  component) is enslaved by the drifting vortex pattern, hence we see here  $\omega_f \sim \omega_v$ . Connected with the linear frequency relationship in this regime we observe a parabolic shape of the growth rate, with a maximum close to the resonance point where the vortex drift frequency would roughly correspond to the eigenfrequency of the magnetic field for the unperturbed, axisymmetric flow, and a quadratic reduction of the growth rate nearby this point. Outside of the resonant regime the field amplitude and the field drift are modulated with twice the frequency of the vortex drift.

The simulations presented in this study show similarities with the results presented in [16] where dynamo action was examined using a flow field obtained from non-linear simulations of spherical  $s2t2$  flow in a sphere. Kinematic dynamo simulations using the time averaged flow or different snapshots of the velocity field did not exhibit dynamo action, whereas this was indeed the case when considering the time-dependent flow. The exclusive occurrence of dynamo action with a time-dependent flow was interpreted as dynamo action based on *non-normal growth* originally described in [51]. The essential prerequisite for non-normal growth is an appropriate mixing of (non-orthogonal) eigenstates through a time dependent linear operator which can lead to growing modes even if the contributing eigenstates alone correspond to decaying solutions in a stationary system. However, we observe a resonant behavior even in runs without equatorial symmetry breaking and with stationary vortices, i.e. in systems without any time dependence so that no time-dependent contribution is available that may provide for a mixture of non-normal modes. Hence, the role of non-normal growth in our models and the comparability with the model of [16] must for now remain an open question.

It is difficult to conclude, if the resonance effect can be realized in existing dynamo experiments. Although a coincidence of forcing frequency (the frequency of the drift motion) and magnetic field frequency cannot be ruled out, the resonance condition is a quite particular case and most probably can only be fulfilled by chance. This is particularly true in the case of a more realistic non-linear analysis, in which the Navier-Stokes- and the induction equation are coupled so that the drift of the vortex pattern might strongly be influenced by back-reaction of the magnetic field. Furthermore, in the examined VKS-like configuration, the vortex drift frequencies observed in the water experiment are far away from the resonance condition (at least for reasonable values of the equatorial symmetry breaking) so that it is unlikely that the vortices affect the VKS dynamo in its actual set-up. Nevertheless, it might be suggestive to change the large scale flow geometry in order to adjust the relation of vortex drift and field drift, e.g. by changing the aspect ratio [52] or by fixing the vortices using some wall inhomogeneity.

The occurrence of parametric resonances might also play a role for future laboratory dynamos, like the large scale precession dynamo scheduled at the Helmholtz-Zentrum Dresden-Rossendorf (HZDR) [53]. It is already well known from preliminary water experiments that drifting non-axisymmetric vortices aligned with the symmetry axis



of the cylindrical container emerge prior to an abrupt transition to turbulence [54]. In the appropriate regime, that means with suitable vortex drift frequencies and perturbation amplitudes, a parametric resonance similar to the effect examined in this study can be useful for increasing the efficiency of the dynamo process. Such effects indeed have been suggested for the Earth's core flow where, however, parametric instabilities caused by tidal forcing may provide the required periodic forcing [55].

## ACKNOWLEDGMENTS

AG and FS acknowledge helpful discussions with Oleg Kirillov and financial support from Deutsche Forschungsgemeinschaft (DFG) in frame of the Collaborative Research Center (SFB) 609. JB is grateful for support of the Spanish government through contract FIS2011-24642. The authors thank B. Knaepen and D. Carati of the Université Libre de Bruxelles for inviting them to the Brussels Summer program 2009. The computations were performed using GPUs provided by the CUDA Research Center at TU Dresden (now CUDA Center of Excellence <http://ccoe-dresden.de>).

- 
- [1] F. Stefani, A. Gailitis, and G. Gerbeth, *Z. Angew. Math. Mech.* **88**, 930 (2008)
  - [2] A. Gailitis, O. Lielausis, S. Dement'ev, E. Platadis, A. Ciferri, G. Gerbeth, T. Gundrum, F. Stefani, M. Christen, H. Hänel, and G. Will, *Phys. Rev. Lett.* **84**, 4365 (2000)
  - [3] R. Stieglitz and U. Müller, *Phys. Fluids* **13**, 561 (2001)
  - [4] R. Monchaux, M. Berhanu, M. Bourgoin, M. Moulin, P. Odier, J.-F. Pinton, R. Volk, S. Fauve, N. Mordant, F. Pétrélis, A. Chiffaudel, F. Daviaud, B. Dubrulle, C. Gasquet, L. Marié, and F. Ravelet, *Phys. Rev. Lett.* **98**, 044502 (2007)
  - [5] M. L. Dudley and R. W. James, *Proc. R. Soc. Lond. A* **425**, 407 (1989)
  - [6] P. Odier, J.-F. Pinton, and S. Fauve, *Phys. Rev. E* **58**, 7397 (1998)
  - [7] C. B. Forest, R. A. Bayliss, R. D. Kendrick, M. D. Nornberg, R. O'Connell, and E. J. Spence, *Magnetohydrodynamics* **38**, 107 (2002)
  - [8] L. Marié, J. Burguete, F. Daviaud, and J. Léorat, *Eur. J. Mech. B* **33**, 469 (2003)
  - [9] M. Bourgoin, R. Volk, P. Frick, S. Khripchenko, P. Odier, and J.-F. Pinton, *Magnetohydrodynamics* **40**, 3 (2004)
  - [10] F. Stefani, M. Xu, G. Gerbeth, F. Ravelet, A. Chiffaudel, F. Daviaud, and J. Léorat, *Eur. J. Mech. B* **25**, 894 (Nov. 2006)
  - [11] F. Ravelet, A. Chiffaudel, F. Daviaud, and J. Léorat, *Phys. Fluids* **17**, 7104 (Nov. 2005)
  - [12] M. Berhanu, R. Monchaux, S. Fauve, N. Mordant, F. Pétrélis, A. Chiffaudel, F. Daviaud, B. Dubrulle, L. Marié, F. Ravelet, M. Bourgoin, P. Odier, J.-F. Pinton, and R. Volk, *Europhys. Lett.* **77**, 59001 (2007)
  - [13] C. Gissinger, A. Isakov, S. Fauve, and E. Dormy, *Europhys. Lett.* **82**, 29001 (2008)
  - [14] C. Gissinger, E. Dormy, and S. Fauve, *Phys. Rev. Lett.* **101**, 144502 (2008)
  - [15] K. Reuter, F. Jenko, and C. B. Forest, *New J. Phys.* **11**, 013027 (2009)
  - [16] K. Reuter, F. Jenko, A. Tilgner, and C. B. Forest, *Phys. Rev. E* **80**, 056304 (2009)
  - [17] R. Monchaux, M. Berhanu, S. Aumaitre, A. Chiffaudel, F. Daviaud, B. Dubrulle, F. Ravelet, S. Fauve, N. Mordant, F. Pétrélis, M. Bourgoin, P. Odier, J.-F. Pinton, N. Plihon, and R. Volk, *Phys. Fluids* **21**, 035108 (2009)
  - [18] P. H. Roberts, G. A. Glatzmaier, and T. L. Chune, *Geophys. Astrophys. Fluid Dyn.* **104**, 207 (2010)
  - [19] I. V. Khalzov, B. P. Brown, F. Ebrahimi, D. D. Schnack, and C. B. Forest, *Phys. Plasmas* **18**, 032110 (2011)
  - [20] E. J. Kaplan, M. M. Clark, M. D. Nornberg, K. Rahbarnia, A. M. Rasmus, N. Z. Taylor, C. B. Forest, and E. J. Spence, *Phys. Rev. Lett.* **106**, 254502 (2011)
  - [21] A. Giesecke, F. Stefani, and G. Gerbeth, *Phys. Rev. Lett.* **104**, 044503 (2010)
  - [22] A. Giesecke, C. Nore, F. Stefani, G. Gerbeth, J. Léorat, W. Herreman, F. Luddens, and J.-L. Guermond, *New J. Phys.* **14**, 053005 (2012)
  - [23] A. de La Torre and J. Burguete, *Phys. Rev. Lett.* **99**, 054101 (2007)
  - [24] F. Ravelet, A. Chiffaudel, and F. Daviaud, *J. Fluid Mech.* **601**, 339 (2008)
  - [25] P.-P. Cortet, P. Diribarne, R. Monchaux, A. Chiffaudel, F. Daviaud, and B. Dubrulle, *Phys. Fluids* **21**, 025104 (2009)
  - [26] J. Burguete and A. De La Torre, *Int. J. Bifurcation Chaos* **19**, 2695 (2009), ISSN 0218-1274
  - [27] T. Kato, *Perturbation theory of linear operators* (Springer, New York, 1966)
  - [28] M. V. Berry, *Czech. J. Phys.* **54**, 1039 (2004)
  - [29] J.-S. Chen and D. B. Bogy, *J. Appl. Mech.* **59**, 390 (1992)
  - [30] R. S. Mackay and P. G. Saffman, *Proc. R. Soc. Lond. A* **406**, 115 (1986)
  - [31] M. Chiba and M. Tosa, *Mon. Not. R. Astr. Soc.* **244**, 714 (1990)
  - [32] D. Schmitt and G. Rüdiger, *Astron. Astrophys.* **264**, 319 (1992)
  - [33] D. Moss, *Astron. Astrophys.* **308**, 381 (1996)
  - [34] R. Rohde, G. Rüdiger, and D. Elstner, *Astron. Astrophys.* **347**, 860 (1999)
  - [35] D. Sokoloff and N. Piskunov, *Mon. Not. R. Astr. Soc.* **334**, 925 (2002)
  - [36] A. de La Torre, J. Burguete, and C. Pérez-García, *Eur. Phys. J. ST* **146**, 313 (2007)
  - [37] A. Isakov and E. Dormy, *Geophys. Astrophys. Fluid Dyn.* **99**, 481 (2005)



- [38] A. Giesecke, F. Stefani, and G. Gerbeth, *Magnetohydrodynamics* **44**, 237 (2008)
- [39] L. Marié, C. Normand, and F. Daviaud, *Phys. Fluids* **18**, 017102 (2004)
- [40] C. Gissinger, *Europhys. Lett.* **87**, 39002 (2009)
- [41] See Supplemental Material at [*URL will be inserted by publisher*] for a movie that shows the temporal field behavior for unperturbed, resonant and modulated cases
- [42] U. Günther, F. Stefani, and G. Gerbeth, *Czech. J. Phys.* **54**, 1075 (2004)
- [43] O. Kirillov, *Fortschritte der Physik*, 2012, ISSN 1521-3978, <http://dx.doi.org/10.1002/prop.201200068>
- [44] B. Dietz, T. Friedrich, J. Metz, M. Miski-Oglu, A. Richter, F. Schäfer, and C. A. Stafford, *Phys. Rev. E* **75**, 027201 (2007)
- [45] M. Henriot, J. Burguete, and R. Ribotta, *Phys. Rev. Lett.* **91**, 104501 (2003)
- [46] F. Stefani and G. Gerbeth, *Phys. Rev. E* **67**, 027302 (2003)
- [47] A. Giesecke, F. Stefani, and G. Gerbeth, *Geophys. Astrophys. Fluid Dynam.*(2012), doi:10.1080/03091929.2012.668543
- [48] J. Priede, R. Avalos-Zuñiga, and F. Plunian, *Physics Letters A* **374**, 584 (2010)
- [49] D. D. Joseph, *Stability of fluid motions I* (Springer, Berlin, 1976)
- [50] J. Guckenheimer and P. Holmes, *Nonlinear Oscillations, Dynamical Systems and Bifurcations of Vector Fields* (Springer, Berlin, 2002)
- [51] A. Tilgner, *Phys. Rev. Lett.* **100**, 128501 (2008)
- [52] K. M. Kuzanyan and D. D. Sokoloff, *Astrophysics and Space Science* **208**, 245 (1993)
- [53] F. Stefani, S. Eckert, G. Gerbeth, A. Giesecke, T. Gundrum, C. Steglich, T. Weier, and B. Wustmann, *Magnetohydrodynamics* **48**, 103 (2012)
- [54] W. Mouhali, *Transition vers la turbulence et applications à l'effect dynamo*, Ph.D. thesis, Université de Paris VII (2009), <http://tel.archives-ouvertes.fr/docs/00/49/04/77/PDF/Manuscritfinal.pdf>
- [55] K. Aldridge, R. Baker, and D. McMillan, *Geophys. Astrophys. Fluid Dyn.* **101**, 507 (2007)